Hypersonic Viscous Shock-Layer Solutions over Long Slender Bodies—Part I: High Reynolds Number Flows

R. N. Gupta* and K. P. Lee†
Scientific Research and Technology, Inc., Hampton, Virginia 23666-1325
and
E. V. Zoby,‡ J. N. Moss,‡ and R. A. Thompson§
NASA Langley Research Center, Hampton, Virginia 23665-5225

Numerical solutions from the time-steady viscous shock-layer (VSL) equations are presented for the hypersonic laminar and turbulent flow of a perfect gas over long slender bodies. These results are obtained from a spatial-marching, implicit, finite-difference technique, which includes coupling of the normal momentum and continuity equations and use of the Vigneron pressure condition in the subsonic nose region. Detailed comparisons have been made with other predictions and experimental data to assess the accuracy of the present numerical technique, especially for slender-body flows. The comparisons have been shown to yield accurate results. Two widely used algebraic turbulence models, namely the Cebeci-Smith (CS) and the Baldwin-Lomax (BL) models, have been analyzed with the present technique for application to long, slender bodies. The BL model has been modified in the present work for pressure-gradient effects and applied successfully at hypersonic flow conditions. Both of these models have been shown to result in similar heating predictions for the attached flows analyzed here.

Nomenclature

A^+ = damping factor in Cebeci-Smith (CS) model
$\tilde{A}^+$ = damping factor in Baldwin-Lomax (BL) model
a = speed of sound
C_{CP} = coefficient used in Baldwin-Lomax (BL) model
C_p^* = specific heat at constant pressure
$F_{\max}$ = maximum of function $F(\bar{\eta})$ in Baldwin-Lomax (BL) model
g = stretching function
H = enthalpy, h^*/U_∞^{*2}
H^* = $h^* + u^{*2}/2$
H_t = total enthalpy, $h + v^2/2$
h = static enthalpy, h^*/U_∞^{*2}
K = thermal conductivity, $K^*/\mu_{\text{ref}}^* C_{p,\infty}^*$
K^* = thermal conductivity
K_T^* = eddy thermal conductivity
ℓ = mixing length
M_∞ = freestream Mach number
M_ξ = local Mach number
n = coordinate measured normal to the body, n^*/R_N^*
n^+ = normal coordinate in turbulence model
Pr = Prandtl number, $C_p^*\mu^*/K^*$
Pr,t = turbulent Prandtl number, $C_p^*\mu_T^*/K^*$
p^+ = pressure-gradient parameter
p = pressure, $p^*/(\rho_\infty^* U_\infty^{*2})$
q = heat-transfer rate, $q^*/(\rho_\infty^* U_\infty^{*3})$
q_{ref}^* = reference heat-transfer rate
Re_∞ = freestream Reynolds number, $\rho_\infty^* U_\infty^* R_N^*/\mu_\infty^*$
R_N^* = body nose radius
r = radius measured from axis of symmetry to a point on the body surface, r^*/R_N^*
St = Stanton number, $= -q_w/(H_\infty - H_w)$
s = coordinate measured along the body surface, s^*/R_N^*
T = temperature, T^*/T_{ref}^*
T_{ref}^* = $U_\infty^{*2}/C_{p,\infty}^*$
U_∞^* = freestream velocity
u = velocity component tangent to body surface, u^*/U_∞^*
u_τ = friction velocity
v = velocity component normal to body surface, v^*/U_∞^*
W = dummy variable used in Eq. (1)
x = axial distance
α = shock angle defined in Fig. 1
$\bar{\alpha}$ = mesh refinement parameter
$\alpha_1, \alpha_2, \alpha_3, \alpha_4$ = coefficients in Eq. (1)
β = angle defined in Fig. 1
$\bar{\beta}$ = mesh refinement parameter
γ = ratio of specific heats
$\gamma_{i,\bar{\eta}}$ = normal intermittency factor
δ = boundary-layer thickness
δ_k = incompressible displacement thickness
ϵ = Reynolds number parameter, $= [\mu_{\text{ref}}^*/\rho_\infty^* U_\infty^* R_N^*]^{1/2}$
ϵ^+ = normalized eddy viscosity, μ_T/μ

Presented as Paper 87-2487 at the AIAA Atmospheric Flight Mechanics Conference, Monterey, CA, August 17-19, 1987; received June 26, 1989; revision received Sept. 5, 1989.

*President. Associate Fellow AIAA.
†Research Engineer. Member AIAA.
‡Research Engineer, Aerothermodynamics Branch, Space Systems Division. Associate Fellow AIAA.
§Research Engineer, Aerothermodynamics Branch, Space Systems Division.

ϵ_i^+ = eddy viscosity from inner law
ϵ_0^+ = eddy viscosity from outer law
η = transformed $\bar{\eta}$ coordinate, $g(\bar{\eta})$
$\bar{\eta}$ = transformed n coordinate, n/n_{sh}
$\bar{\eta}_{max}$ = value of $\bar{\eta}$ at which $F(\bar{\eta})$ is maximum
$\Delta\bar{\eta}_1$ = step size adjacent to the surface
θ = body angle defined in Fig. 1
κ = body curvature, $\kappa^* R_N^*$
ω = vorticity
μ = viscosity, μ^*/μ_{ref}^*
μ_T = eddy viscosity
μ_{ref}^* = reference viscosity, $\mu^*(T_{ref}^*)$
ξ = coordinate measured along the body surface, $=s$
$\Delta\xi_1$ = step-size adjacent to the stagnation streamline
ρ = density, ρ^*/ρ_∞^*
τ = shear stress, $\tau^*/(\rho_\infty^* U_\infty^{*2})$

Subscripts

e = boundary-layer edge
sh = shock value
w = wall value
∞ = freestream value

Superscripts

j = zero for plane flow and one for axisymmetric flow
$\sim$ = shock-oriented velocity components
$'$ = total differential
$*$ = dimensional quantity

Introduction

RECENTLY, there has been a resurgence of interest in hypersonic aerothermodynamics. This has been motivated by the currently envisaged transatmospheric vehicles.[1,2] The calculation of hypersonic viscous flowfields past long slender axisymmetric blunt bodies is of prime interest to the designer of such re-entry aerospace vehicles. A variety of flow conditions are encountered during the transatmospheric flight of these vehicles. Therefore, the solutions to the flowfield equations are required over a wide range of Reynolds numbers, ranging from low Reynolds numbers at high altitudes to high Reynolds numbers at low altitudes. In this paper, attention will be restricted to flowfield analysis for the high Reynolds number case. The low Reynolds number flow with recently obtained surface- and shock-slip boundary conditions has been analyzed in Ref. 3.

In the past, three basic approaches have been employed for analyzing the hypersonic flow past axisymmetric blunt bodies. They range from using second-order boundary-layer equations[4,5] to the more complex Navier-Stokes equations.[6,7] The viscous shock-layer (VSL) equations[8] represent an intermediate level of approximation. Methods based on the coupling of the viscous boundary-layer solutions and the outer inviscid Euler solutions are not uniformly applicable across the shock layer and are approximate in nature. In addition, the excessive computing times and computer storage requirements make the Navier-Stokes solutions less appealing for long bodies and parametric studies.

The VSL equations are obtained from the full Navier-Stokes equations by keeping terms up to second order in the inverse square root of the Reynolds number in both viscous and inviscid regions. This process results in one set of equations uniformly valid throughout the shock layer, and viscous-inviscid interactions are accounted for in a straightforward manner. The VSL equations can provide solutions for flows over slender long bodies (where strong vorticity interactions occur far downstream) without excessive computer time or storage requirements. In contrast with the parabolized Navier-Stokes (PNS) solutions,[9-11] the VSL solutions do not use any smoothing procedures that damp out numerical oscillations and are self starting for blunt-body application. The smoothing terms add artificial viscosity to the solutions, which can distort the exact solutions.[12]

The steady-state VSL equations are of mixed hyperbolic-elliptic type in the subsonic nose region of a blunt body and are of mixed hyperbolic-parabolic type in the supersonic region. With the elimination of the streamwise diffusion terms, the streamwise gradients of the pressure and normal velocity cause the VSL equations to be elliptic in the subsonic region. To overcome this elliptic (or boundary value) nature of the problem in the streamwise direction, Davis[8] obtained solutions of the full VSL equations by relaxing the shock shape obtained from the thin-layer solution. In addition, Davis[8] solved the VSL governing equations in a successive manner, and this approach results in a divergent solution for slender bodies.

Werle et al.[13] introduced an artificial time coordinate to relax the shock from an initial shape. Even with this relaxation scheme, difficulties were experienced with long, slender blunt bodies. The difficulties encountered in Ref. 13 were associated with the first-order continuity and the normal momentum equations, and a coupling of these two equations was suggested in the solution procedure. Waskiewicz et al.[14] successfully implemented this suggestion for slender blunt bodies less than 20 nose radii in length. Their VSL code, which was later extended to three-dimensional flows (VSL3D) in Ref. 15, was recently employed by Thompson et al.[16] to analyze flows past long slender conical vehicles. However, both in Refs. 14 and 16, a smaller streamwise step-size ($s/R_N < 0.1$) could not be employed successfully in the subsonic nose region.

Hosny et al.[17] and Gordon and Davis[18] have solved the governing equations as a fully coupled set. Coupling the equation for shock standoff distance does result in a convergence problem in Ref. 18. A relaxation scheme is used there for updating the shock standoff distance after each global pass, and the first streamwise derivative of the shock standoff distance is taken from the previous global iteration to overcome the convergence problem.

In this paper, a method is presented for solving flow over a long, blunted slender body where the inviscid region encompasses a significant portion of the total shock-layer thickness. The first-order continuity and normal momentum equations are solved simultaneously as in Ref. 14 rather than in a successive manner as has been utilized[8,19] for wide-angle bodies. Also, based on the studies of Refs. 20 and 21, the Vigneron condition is employed for the streamwise pressure gradient in the subsonic nose region. The enhanced flowfield stability and convergence based on these assumptions is illustrated by comparisons with solution techniques that do not utilize these options (e.g., Ref. 19). In addition, results of the present method are compared with a wide range of experimental data and solutions of other detailed methods.

The present work also includes the use of two of the most frequently employed algebraic turbulence models, namely, the Cebeci-Smith (CS) and Baldwin-Lomax (BL) models. The application of the models to hypersonic-attached flow conditions

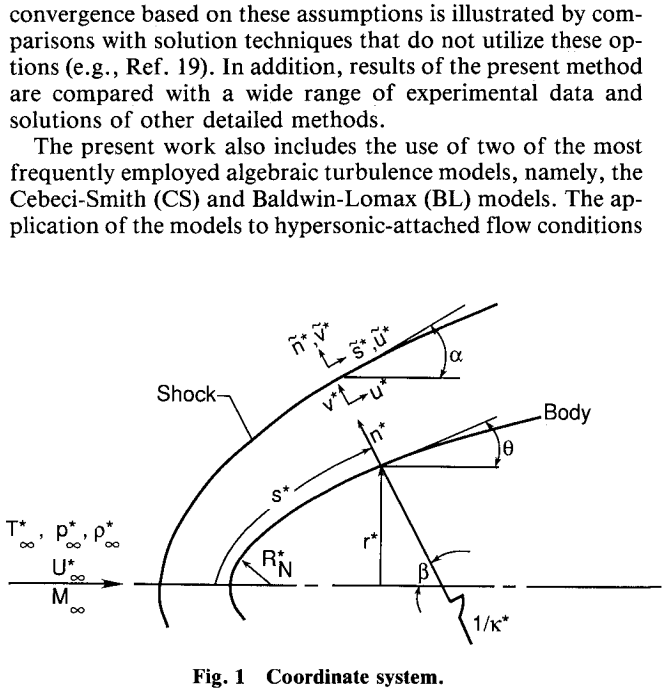

Fig. 1 Coordinate system.

with pressure gradients over slender sphere cones is examined and compared with the available experimental data.

Analysis

Governing Equations

The conservation equations employed in the present analysis are the steady, perfect-gas VSL equations[8,19] for an axisymmetric or two-dimensional body at zero deg angle of attack (see Fig. 1). For turbulent flow, time-averaged quantities are implied by the nomenclature of Ref. 19, and the laminar-flow equations are obtained by neglecting the turbulent contributions. These equations in the orthogonal, body-oriented, transformed coordinates and nondimensional form are provided here. The second-order partial differential equations are written in the following form:

$$\frac{\partial^2 W}{\partial \eta^2} + \frac{(\partial^2 g/\partial \bar{\eta}^2) + \alpha_1(\partial g/\partial \bar{\eta})}{(\partial g/\partial \bar{\eta})^2}\frac{\partial W}{\partial \eta} + \frac{\alpha_2}{(\partial g/\partial \bar{\eta})^2} W + \frac{\alpha_3}{(\partial g/\partial \bar{\eta})^2} + \frac{\alpha_4}{(\partial g/\partial \bar{\eta})^2}\frac{\partial W}{\partial \xi} = 0 \tag{1}$$

where $\partial g/\partial \bar{\eta}$ and $\partial^2 g/\bar{\eta}^2$ are the first and second derivatives of the stretching function $g(\bar{\eta})$. The quantity W represents u in the s-momentum equation and H in the energy equation. The coefficients α_1 to α_4 are written as follows:

s-momentum, $W = u$:

$$\alpha_1 = \frac{1}{\mu(1+\epsilon^+)}\frac{\partial \mu(1+\epsilon^+)}{\partial \eta}\frac{\partial g}{\partial \bar{\eta}} + \frac{n_{sh}\kappa(1+2\epsilon^+)}{(1+\bar{\eta}n_{sh}\kappa)(1+\epsilon^+)} + \frac{jn_{sh}\cos\theta}{r+\bar{\eta}n_{sh}\cos\theta} + \frac{n'_{sh}n_{sh}\bar{\eta}\rho u}{\epsilon^2\mu(1+\epsilon^+)(1+\bar{\eta}n_{sh}\kappa)} - \frac{n_{sh}\rho v}{\epsilon^2\mu(1+\epsilon^+)} \tag{2a}$$

$$\alpha_2 = -\frac{n_{sh}\kappa}{\mu(1+\epsilon^+)(1+\bar{\eta}n_{sh}\kappa)}\frac{\partial \mu(1+\epsilon^+)}{\partial \eta}\frac{\partial g}{\partial \bar{\eta}} - \frac{n_{sh}^2\kappa}{(1+\epsilon^+)(1+\bar{\eta}n_{sh}\kappa)} \times \left[\frac{\kappa}{1+\bar{\eta}n_{sh}\kappa} + \frac{j\cos\theta}{r+\bar{\eta}n_{sh}\cos\theta}\right] - \frac{n_{sh}^2\kappa\rho v}{\epsilon^2(1+\bar{\eta}n_{sh}\kappa)\mu(1+\epsilon^+)} \tag{2b}$$

$$\alpha_3 = -\frac{n_{sh}^2}{\epsilon^2(1+\bar{\eta}n_{sh}\kappa)\mu(1+\epsilon^+)}\left[\frac{\partial p}{\partial \xi} - \frac{n'_{sh}\bar{\eta}}{n_{sh}}\frac{\partial g}{\partial \bar{\eta}}\frac{\partial p}{\partial \eta}\right] \tag{2c}$$

$$\alpha_4 = -\frac{n_{sh}^2\rho u}{\epsilon^2(1+\bar{\eta}n_{sh}\kappa)\mu(1+\epsilon^+)} \tag{2d}$$

Energy, $W = H$:

$$\alpha_1 = \left\{1\Big/\left[\frac{\mu}{Pr}\left(1+\epsilon^+\frac{Pr}{Pr,t}\right)\right]\right\}\frac{\partial g}{\partial \bar{\eta}}\frac{\partial}{\partial \eta}\left[\frac{\mu}{Pr}\left(1+\epsilon^+\frac{Pr}{Pr,t}\right)\right] + \frac{\kappa n_{sh}}{1+\bar{\eta}n_{sh}\kappa} + \frac{jn_{sh}\cos\theta}{r+\bar{\eta}n_{sh}\cos\theta} + \frac{n'_{sh}n_{sh}\bar{\eta}\rho u}{\epsilon^2\dfrac{\mu}{Pr}\left(1+\epsilon^+\dfrac{Pr}{Pr,t}\right)(1+\bar{\eta}n_{sh}\kappa)} - \frac{n_{sh}\rho v}{\epsilon^2\dfrac{\mu}{Pr}\left(1+\epsilon^+\dfrac{Pr}{Pr,t}\right)} \tag{3a}$$

$$\alpha_2 = 0 \tag{3b}$$

$$\alpha_3 = \frac{n_{sh}}{\dfrac{\mu}{Pr}\left(1+\epsilon^+\dfrac{Pr}{Pr,t}\right)}\left[\frac{\partial g}{\partial \bar{\eta}}\frac{\partial \Phi}{\partial \eta} + n_{sh}\left(\frac{\kappa}{1+\bar{\eta}n_{sh}\kappa} + \frac{j\cos\theta}{r+\bar{\eta}n_{sh}\cos\theta}\right)\Phi + \frac{v}{\epsilon^2}\frac{\partial g}{\partial \bar{\eta}}\frac{\partial p}{\partial \eta} - \frac{n_{sh}\kappa v\rho u^2}{\epsilon^2(1+\bar{\eta}n_{sh}\kappa)}\right] \tag{3c}$$

$$\alpha_4 = -\frac{n_{sh}^2\rho u}{\epsilon^2\dfrac{\mu}{Pr}\left(1+\epsilon^+\dfrac{Pr}{Pr,t}\right)(1+\bar{\eta}n_{sh}\kappa)} \tag{3d}$$

where

$$\Phi = \frac{\mu}{Pr}\left[Pr - 1 + \epsilon^+\frac{Pr}{Pr,t}(Pr,t-1)\right]\frac{u}{n_{sh}}\frac{\partial g}{\partial \bar{\eta}} \times \frac{\partial u}{\partial \eta} - \frac{\mu u^2\kappa}{(1+\bar{\eta}n_{sh}\kappa)} \tag{3e}$$

The remaining first-order equations are written as follows.

Global continuity:

$$\frac{\partial}{\partial \xi}\left[n_{sh}(r+\bar{\eta}n_{sh}\cos\theta)^j\rho u\right] + \frac{\partial g}{\partial \bar{\eta}}\frac{\partial}{\partial \eta}\left\{(r+\bar{\eta}n_{sh}\cos\theta) \times \left[(1+\bar{\eta}n_{sh}\kappa)\rho v - n'_{sh}\bar{\eta}\rho u\right]\right\} = 0 \tag{4}$$

n-momentum:

$$\frac{\rho u}{(1+\bar{\eta}n_{sh}\kappa)}\frac{\partial v}{\partial \xi} - \frac{n'_{sh}\bar{\eta}\rho u}{n_{sh}(1+\bar{\eta}n_{sh}\kappa)}\frac{\partial v}{\partial \eta}\frac{\partial g}{\partial \bar{\eta}} + \frac{\rho v}{n_{sh}}\frac{\partial v}{\partial \eta}\frac{\partial g}{\partial \bar{\eta}} - \frac{\rho u^2\kappa}{(1+\bar{\eta}n_{sh}\kappa)} + \frac{1}{n_{sh}}\frac{\partial p}{\partial \eta}\frac{\partial g}{\partial \bar{\eta}} = 0 \tag{5}$$

$$p = \rho T(\gamma+1)/\gamma \tag{6}$$

In Eqs. (2-5), prime denotes differentiation with respect to ξ. Further, Eqs. (1-5) contain the following independent transformation

$$\eta = g\left(\frac{n}{n_{sh}}\right) = g(\bar{\eta}) \tag{7a}$$

The stretching function $g(\bar{\eta})$ is given by

$$g(\bar{\eta}) = 1 - \left[\bar{\alpha} + \frac{(1-\bar{\alpha})}{\ell n[(\bar{\beta}+1)/(\bar{\beta}-1)]}\ell n\left\{\frac{\bar{\beta}-\bar{\eta}(2\bar{\alpha}+1)+1}{\bar{\beta}+\bar{\eta}(2\bar{\alpha}+1)-1}\right\}\right] \tag{7b}$$

and its first and second derivatives are

$$\frac{dg}{d\bar{\eta}} = \frac{(1-\bar{\alpha})(2\bar{\alpha}+1)}{\ell n[(\bar{\beta}+1)/(\bar{\beta}-1)]}\left\{\frac{1}{[\bar{\beta}-\bar{\eta}(2\bar{\alpha}+1)+1]} + \frac{1}{[\bar{\beta}+\bar{\eta}(2\bar{\alpha}+1)-1]}\right\} \tag{7c}$$

$$\frac{d^2g}{d\bar{\eta}^2} = \frac{(1-\bar{\alpha})(2\bar{\alpha}+1)^2}{\ell n[(\bar{\beta}+1)/(\bar{\beta}-1)]}\left\{\frac{1}{[\bar{\beta}-\bar{\eta}(2\bar{\alpha}+1)+1]^2} - \frac{1}{[\bar{\beta}+\bar{\eta}(2\bar{\alpha}+1)-1]^2}\right\} \tag{7d}$$

Equation (7b) permits the mesh to be refined near the body with $\bar{\alpha}=0$, or refined equally near both the body and shock with $\bar{\alpha}=\frac{1}{2}$ in the physical plane. A value of $\bar{\alpha}=0$ has been

used here, whereas $\bar{\alpha} = \frac{1}{2}$ is more appropriate for the low-density flows.[3] Parameter $\bar{\beta}$ controls the amount of refinement with values near 1 giving the largest amount of stretching. Equation (7a) may be inverted to obtain the physical coordinate $\bar{\eta}$ from the transformed η coordinate.

$$\bar{\eta} = \frac{1}{(2\bar{\alpha}+1)}\left[1-\bar{\beta}\left\{\frac{[(\bar{\beta}+1)/(\bar{\beta}-1)]^{(1-\eta-\bar{\alpha})/(1-\bar{\alpha})}-1}{[(\bar{\beta}+1)/(\bar{\beta}-1)]^{(1-\eta-\bar{\alpha})/(1-\bar{\alpha})}+1}\right\}\right] \quad (7e)$$

The transformation of Eq. (7a) insures a uniform mesh in the computational coordinate.

For the present study, the molecular and turbulent Prandtl numbers are assumed to be 0.71 and 0.9, respectively. The molecular viscosity is computed with the Sutherland relation.

Boundary Conditions

The boundary conditions at the shock are calculated by using the Rankine-Hugoniot relations.[8] At the wall, the no-slip and no-temperature-jump boundary conditions are used. The wall temperature and enthalpy are specified as constant for the present study.

For ease in numerical computations, Eqs. (1-6) as well as the boundary conditions are further transformed by normalizing the variables with their local shock values. The normal velocity v is not normalized because this quantity can change sign at the shock and can be near zero. Therefore, the normalized v profiles may not be well behaved.

Turbulence Models

In this study, two widely used algebraic turbulence models, namely, the CS[22] and BL,[23] have been analyzed for application to attached flow over long, slender bodies. In a recent study of supersonic flow past an ogive-cylinder-boattail projectile, Danberg et al.[24] demonstrated that use of the CS algebraic model gave results comparable to the more detailed k-ϵ model of Jones and Launder.[25] Algebraic turbulence models are more appealing since they require less computer storage and much less computational time as compared to the two-equation (such as k-ϵ) model of turbulence.

The BL turbulence model was initially developed based on the CS model with modifications that avoid the necessity for determining the edge of the boundary layer. In the BL model, the maximum in the vorticity function is used to define the length scale for the outer layer. However, the present study and that of Ref. 26 observed that two peaks in the vorticity distribution can result, and care must be taken to select the correct peak. Further, some of the constants for the outer layer expression in the BL turbulence model were initially obtained by requiring agreement with the Cebeci formulation for constant pressure boundary layers at transonic speeds. A recent study[27] implied that one of the constants may depend on Mach number.

Both the BL and CS models of turbulence employ a two-layer eddy-viscosity formulation. The inner law is based on Prandtl's mixing-length concept. The outer law employs either the Clauser-Klebanoff expression in the CS model or an equivalent expression in the BL model for computing the eddy viscosity. In both of these turbulence models, the eddy viscosity degenerates to approximately zero in the inviscid portion of the shock layer.

Cebeci-Smith Turbulence Model

The algebraic eddy viscosity (in nondimensional form) is given by

$$\epsilon^+ = \begin{cases} \epsilon_i^+ & \bar{\eta} \le \bar{\eta}_{\text{crossover}} \\ \epsilon_0^+ & \bar{\eta} > \bar{\eta}_{\text{crossover}} \end{cases} \quad (8)$$

The $\bar{\eta}_{\text{crossover}}$ is the value of $\bar{\eta}$ at which values from the inner and outer formulas are equal.

The inner eddy viscosity is obtained from the Prandtl mixing-length concept

$$\epsilon_i^+ = \frac{\rho \ell^2}{\epsilon^2 \mu}\frac{1}{n_{sh}}\left|\frac{\partial u}{\partial \eta}\frac{\partial g}{\partial \bar{\eta}}\right| \quad (9)$$

The mixing length ℓ is obtained by using the Van Driest proposal stated as[22]

$$\ell = K_1 n_{sh}\bar{\eta}\left[1-\exp(-n^+/A^+)\right] \quad (10)$$

where

$$n^+ = \frac{n_{sh}\bar{\eta}\rho}{\epsilon\mu}\left[\frac{\mu_w}{\rho n_{sh}}\left(\frac{\partial u}{\partial \eta}\frac{\partial g}{\partial \bar{\eta}}\right)_w\right]^{1/2} \quad (11)$$

Here, K_1 is the von Kármán constant with a value of 0.4, and A^+ is a damping factor expressed (for flows with a pressure gradient) as[22]

$$A^+ = 26(1-11.8P^+)^{-1/2} \quad (12)$$

where

$$P^+ = -\epsilon^2\frac{\mu}{\rho^2 u_\tau^3}\left[\left(\frac{\partial p}{\partial \xi}\right)_e - \frac{n'_{sh}}{n_{sh}}\bar{\eta}_e\left(\frac{\partial g}{\partial \bar{\eta}}\right)_e\left(\frac{\partial p}{\partial \eta}\right)_e\right] \quad (13)$$

$$u_\tau = \epsilon\left[\frac{\mu_w}{\rho n_{sh}}\left(\frac{\partial u}{\partial \eta}\frac{\partial g}{\partial \bar{\eta}}\right)_w\right]^{1/2} \quad (14)$$

$$n'_{sh} = \partial n_{sh}/\partial \xi \quad (15)$$

For the outer region of the viscous layer, the eddy viscosity is approximated by the Clauser-Klebanoff expression[22]

$$\epsilon_0^+ = \frac{K_2 \rho u_e \delta_k \gamma_{i,\bar{\eta}}}{\epsilon^2 \mu} \quad (16)$$

where

$$\delta_k = \int_0^\delta \left(1-\frac{u}{u_e}\right)\frac{n_{sh}}{\partial g/\partial \bar{\eta}}\,d\eta \quad (17)$$

$$K_2 = 0.0168 \quad (18)$$

$$\gamma_{i,\bar{\eta}} = \left[1+5.5\left(\frac{n_{sh}\bar{\eta}}{\delta}\right)^6\right]^{-1} \quad (19)$$

In Eqs. (17) and (19), the boundary-layer thickness δ is assumed to be the value of $\bar{\eta}$ at the point where

$$\frac{H_t}{H_{t,\infty}} = 0.995 \quad (20)$$

With Eq. (20) applied to solutions over long slender bodies, the present study and that of Ref. 16 determined that slight numerical inaccuracies in the flowfield solution resulted in anomalous behavior of the boundary-layer-edge location and in the subsequent heat-transfer and skin-friction distributions. Another criterion for obtaining δ, based on viscous dissipation, is the height where

$$\int_0^\delta \left(\frac{F}{\partial g/\partial \bar{\eta}}\right)d\eta \Big/ \int_0^1 \left(\frac{F}{\partial g/\partial \bar{\eta}}\right)d\eta = 0.995 \quad (21)$$

with

$$F = \left\{\epsilon^2\mu\left[(1+\epsilon^+)\frac{1}{n_{sh}}\frac{\partial g}{\partial \bar{\eta}}\frac{\partial u}{\partial \eta} - \frac{\kappa u}{(1+\bar{\eta}n_{sh}\kappa)}\right]\right\}^2/(1+\epsilon^+)\mu \quad (22)$$

The study of Ref. 16 has recently employed the following criterion

$$d(H_t/H_{t,\infty})/d\bar{\eta} \le 0.5 \quad (23)$$

to define the boundary-layer edge and has demonstrated consistent success in resulting heat-transfer predictions for both short and long blunt bodies.

Both continuous and instantaneous transitions from laminar to turbulent flow have been included in the present investigation. Continuous transition is implemented by defining a streamwise transition intermittency factor[28] $\gamma_{i,\xi}$ which modified the composite eddy viscosity ϵ^+ over a distance interval along the body.

Baldwin-Lomax Turbulence Model

This model employs a formulation similar to the CS model for the inner-region eddy viscosity

$$\epsilon_i^+ = \frac{\rho \ell^2}{\epsilon^2 \mu} |\omega| \tag{24}$$

where ℓ is given by Eq. (10) except that A^+ is replaced by $\tilde{A}^+$, which is defined as

$$\tilde{A}^+ = 26\left(\frac{|\tau|}{\tau_w}\right)^{-1/2} \tag{25}$$

In Eq. (25), τ is the local shear stress obtained from

$$\tau = \epsilon^2 \mu \left[(1+\epsilon^+) \frac{1}{n_{sh}} \frac{\partial g}{\partial \bar{\eta}} \frac{\partial u}{\partial \eta} - \frac{\kappa u}{(1+\bar{\eta} n_{sh} \kappa)} \right] \tag{26}$$

The magnitude of the vorticity $|\omega|$ in Eq. (24) is given by

$$|\omega| = \left| \frac{1}{(1+\bar{\eta} n_{sh} \kappa)} \left[\frac{\partial v}{\partial \xi} - \frac{\bar{\eta} n_{sh}'}{n_{sh}} \frac{\partial g}{\partial \bar{\eta}} \frac{\partial v}{\partial \eta} - \frac{(1+\kappa n_{sh} \bar{\eta})}{n_{sh}} \frac{\partial g}{\partial \bar{\eta}} \frac{\partial u}{\partial \eta} - \kappa u \right] \right| \tag{27}$$

The outer-eddy-viscosity approximation of the BL model replaces the Clauser-Klebanoff formulation by the relation

$$\epsilon_0^+ = \frac{K_2 C_{CP} \rho F_{\text{wake}} F_{\text{KLEB}}(\bar{\eta})}{\epsilon^2 \mu} \tag{28}$$

where K_2 is a constant given by Eq. (19), C_{CP} is an additional constant given as 1.6 in Ref. 23, and

$$F_{\text{wake}} = \bar{\eta}_{\max} F_{\max} \tag{29}$$

The quantities $\bar{\eta}_{\max}$ and $F_{\max}$ are the values at the location of the maximum value in the vorticity function

$$F(\bar{\eta}) = n_{sh} \bar{\eta} |\omega| \left[1 - \exp(-n^+/\tilde{A}^+) \right] \tag{30}$$

The Klebanoff intermittency factor F_{KLEB} is given by

$$F_{\text{KLEB}}(\bar{\eta}) = \left[1 + 5.5\left(\frac{C_{\text{KLEB}} \bar{\eta}}{\bar{\eta}_{\max}}\right)^6 \right]^{-1} \quad \text{with} \quad C_{\text{KLEB}} = 0.3 \tag{31}$$

In Eq. (30), n^+ is given by Eq. (11) and $\tilde{A}^+$ is defined by Eq. (25). Note that Ref. 23 has employed wall values for μ and ρ [appearing in Eq. (11)] in place of the local values used in the CS model. Further, $\tilde{A}^+$ employed in Ref. 23 (defined there as A^+) is used as a constant having a value of 26. These two assumptions of Ref. 23 may be valid for the constant pressure boundary layers analyzed there. For flows with pressure gradients, forms of n^+ and $\tilde{A}^+$ presented in this study are more appropriate.

Further, two different forms of the expression for the damping factor [namely, Eqs. (12) and (25)] have been used in the CS and BL turbulence models for flows with pressure gradient. Equation (12) is employed in the CS model in the inner region only and, therefore, A^+ has been obtained by using τ from the location where the inner and outer eddy viscosity curves intersect. However, Eq. (25) is used in the BL model for damping both the inner and outer region viscosities and, therefore, a local value of τ is employed in obtaining $\tilde{A}^+$.

Method of Solution

General Approach

The overall method of solution employed is an implicit, finite-difference, spatial-matching method similar to the one employed in Refs. 8 and 19. However, the method developed here differs in certain basic respects from that of Refs. 8 and 19. If the method of solution as outlined in these references is employed, convergence problems are encountered with the increasing shock layer thickness. There are two basic reasons for the divergence and instability when using the approach of Refs. 8 and 19 for long slender bodies. First, the governing equations are solved successively, which minimizes the coupling and fails to reflect certain physical interactions. Second, the pressure-gradient term in the streamwise momentum equation is approximated as a hyperbolic term through backward differences in the subsonic nose region. If the initial shock shape is not a good approximation to the final result, departure solutions, similar to the ones noted for the PNS solutions,[20,29,30] may result. These departure solutions are suppressed in Refs. 8 and 19 by taking a step size in the streamwise direction sufficiently large so that the elliptic interaction region is overstepped and by using a good initial guess for the shock shape from the thin VSL solution. However, one should keep in mind that these procedures are not always sufficient to ensure a converged solution. A restriction on initial step size is encountered also in the use of VSL code discussed in Ref. 16, which does not employ the Vigneron condition.[20]

The Vigneron condition[20] is applied to the pressure gradient in the streamwise momentum equation in the present work and has been used to suppress the departure solution. This condition provides the capability to "march" through even a large subsonic region and to use an initial streamwise step size less than the minimum value provided in Ref. 30. Obviously, the step size should not be restricted in order to obtain stable or accurate solutions. Thus, the pressure-gradient term $\partial p/\partial \xi$, which appears in Eq. (2c), may be written with the Vigneron condition as

$$\frac{\partial p}{\partial \xi} = \omega \left(\frac{\partial p}{\partial \xi} \right)_h + (1-\omega) \left(\frac{\partial p}{\partial \xi} \right)_e \tag{32}$$

The term $(\partial p/\partial \xi)_h$ is the "hyperbolic" portion of the pressure gradient, which is backward differenced, and $(\partial p/\partial \xi)_e$ is the "elliptic" portion of the pressure gradient, which is forward differenced to allow for upstream influences. The factor ω is given by

$$\omega = \min\left\{ f(M_\xi), 1 \right\} \tag{33a}$$

and

$$f(M_\xi) = \gamma M_\xi^2 / \left[1 + (\gamma - 1) M_\xi^2 \right] \tag{33b}$$

The Vigneron condition as given by Eq. (32) recognizes that, for a well-posed initial value problem, solutions in the subsonic region can be obtained by marching in the streamwise direction only if a portion $\omega(\partial p/\partial \xi)_h$ of the pressure-gradient term is treated implicitly.

In the present work, Eq. (32) is implemented by specifying $(\partial p/\partial \xi)_e$ at the shock location and keeping it constant across the shock layer at constant ξ values. This is similar to the approach used in Ref. 21. The initial shock shape is created by the thin-layer approximation for a short, wide-angle body (35-deg sphere cone, for example). The shock shape obtained from a full-layer solution to this body shape is then used as an initial guess for the slender bodies in a sequential manner by reducing

the body angles in steps of 5 to 10 deg. With the Vigneron condition employed, a global iteration on the shock shape and, hence, on the quantity $(\partial p/\partial \xi)_e$ is performed in the subsonic nose region. This, in principle, is similar to the global pressure relaxation procedure of Rubin and Lin[31] except that only the pressure at the shock wave location is relaxed in the present approach. This pressure is then used to obtain $(\partial p/\partial \xi)_e$, which is used across the entire shock layer. One may also perform global iterations on the entire pressure field and, hence, use local values for $(\partial p/\partial \xi)_e$ across the shock layer in the subsonic nose region. For the present calculations, the shock shape extending to a location beyond the shock-inflection point is globally iterated. For selected test cases, three global iterations were performed, and discrepancies in the shock standoff distance and its slope in the streamwise direction from the second and third global passes were insignificant (<1%). Downstream of the shock-inflection point (where the shock shape is almost a straight line), the initial shock shape is obtained by linear extrapolation of previous values and is converged by local iterations. The present computational procedure for very long bodies is more time efficient than the approach that globally converges the shock over the entire body. However, for a few conditions of this investigation, the computed shock shape over the entire body was further globally iterated to ascertain convergence of the extrapolated part of the shock shape. No subsequent noticeable changes in the shock parameters or surface measurable quantities were noted.

In the present analysis, the energy equation is formulated in terms of the total enthalpy ($H = h + u^2/2$). This formulation recognizes the dominant role played by the tangential velocity for long slender bodies with large inviscid regions and appears to give enhanced stability and accuracy to the numerical scheme. In the present approach, the derivative of the shock standoff distance is smoothed after each global iteration. In Ref. 16, the shock standoff distance is smoothed after each global iteration. The present approach should result in superior mass conservation. Also, because of the change in sign of the normal velocity profile from station to station, an underrelaxation scheme[32]

$$F = \tilde{\omega}F_1 + (1-\tilde{\omega})F_2 \qquad (34)$$

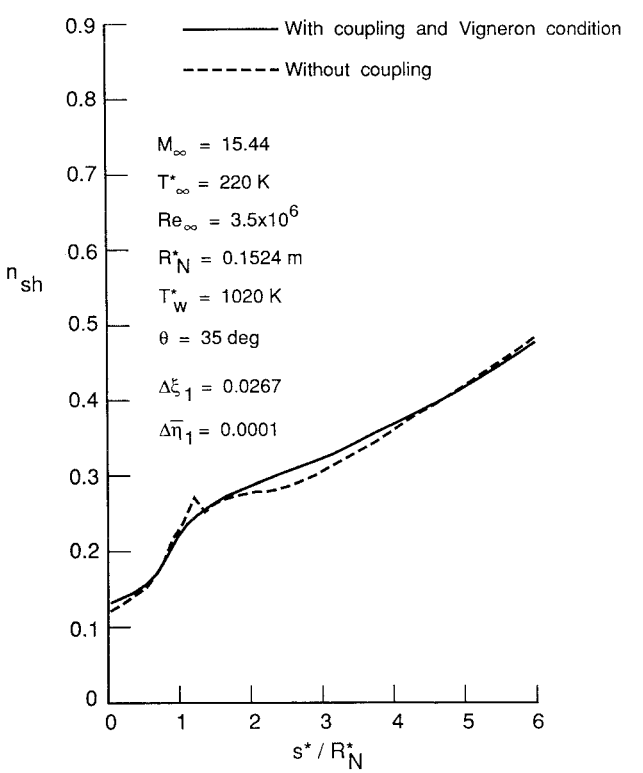

Fig. 2 Shock standoff distance for a 35-deg sphere cone ($\Delta\xi_1$ = 0.0267).

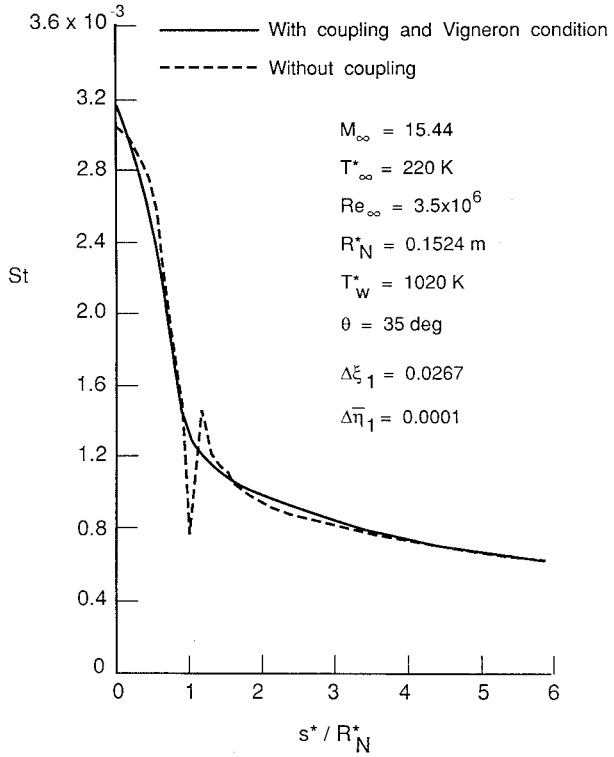

Fig. 3 Stanton number distribution for a 35-deg sphere cone ($\Delta\xi_1$ = 0.0267).

has been employed in the present work. The F_1 is the most recently calculated physical quantity, and F_2 is the value obtained from the previous local iteration or previous station for the first local iteration. A value of $\tilde{\omega}$ of 0.2 to 0.4 gives convergence in most cases. In general, an underrelaxation was required only for the pressure and normal velocity.

Solution Procedure

Let the subscript m denote the station measured along the body surface and n denote the station measured normal to the body surface. The second-order equations (1-3) are replaced with central differences taken in the η direction and two-point backward differences in the ξ direction at the point (m,n). The first-order global continuity equation (4) and n-momentum equation (5) are solved for the pressure p and normal velocity v in a coupled way. The density in these equations is eliminated through the use of equation of state, Eq. (6). Each of the Eqs. (4) and (5) are expressed in finite-difference form at points $(m, n+1/2)$ and $(m, n-1/2)$ using a box scheme discussed by Richtmyer.[33] In these two coupled equations, p and v are eliminated alternatively to solve for these two variables.

The solution is started at the stagnation point where the various flowfield quantities are expanded in terms of the distance ξ along the body surface. These series expansions reduce the partial differential equations (1-5) to ordinary differential equations in terms of η. At a body location m, other than the stagnation point, a two-point backward difference is used for the derivative with respect to ξ at the point (m,n) as mentioned earlier. This again gives ordinary differential equations at location m in terms of η for Eqs. (1-5). The finite-difference forms of these ordinary differential equations (obtained through the central differences) can easily be solved by using the Thomas algorithm.

The solution is iterated at location m until convergence is achieved. The solution advances to the next body station $m+1$ and uses the previous converged solution profiles as initial values for starting the solution at $m+1$. This procedure is repeated until a global solution at all body locations is obtained.

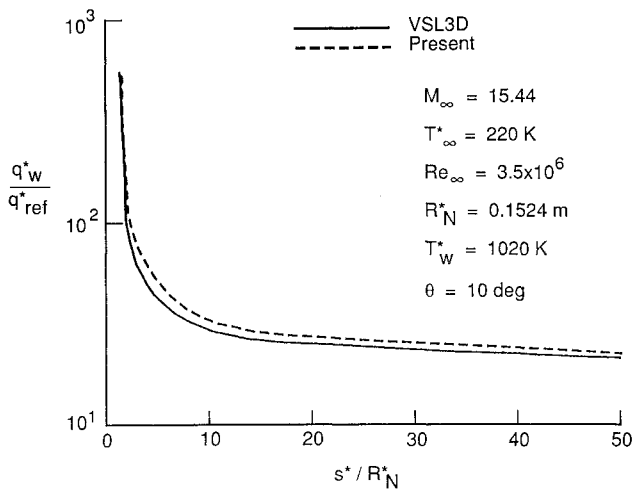

Fig. 4 Surface heat-transfer rate distribution for a 10-deg sphere cone with laminar flow.

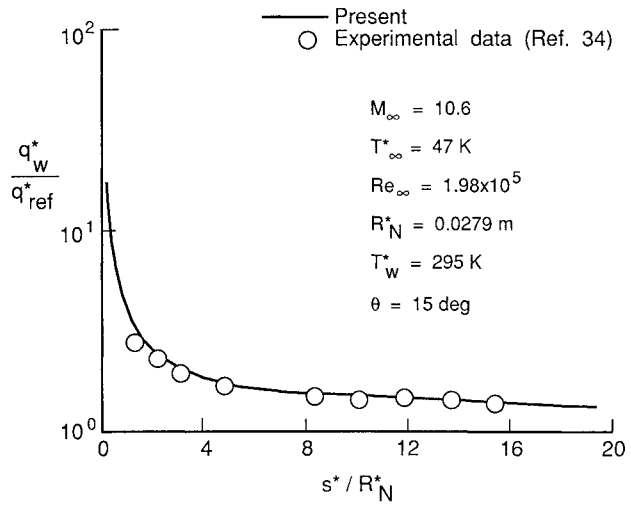

Fig. 5 Surface heat-transfer rate distribution for a 15-deg sphere cone with laminar flow.

Results and Discussion

Numerical solutions with the present VSL method have been obtained for hypersonic flow over a long slender body. Results are for the laminar, transitional, and turbulent hypersonic flow of a perfect gas over slender bodies. The results of the calculations have been compared with experimental data and results of other detailed solutions. A discussion of the comparisons is presented in the following sections.

Laminar Flow Comparisons

Figures 2 and 3 show the shock standoff distance and Stanton number distribution over a 35-deg sphere cone at a Mach number of 15.44 and an initial streamwise normalized step size of 0.0267. The results have been obtained by the method outlined earlier. In this method, where coupling between the normal momentum and continuity equations is implemented, the Vigneron condition is also included. The method without coupling (see Ref. 8) produced results with numerical oscillations at the sphere-cone tangency point as shown by Figs. 2 and 3. For additional global iterations, a divergent solution was obtained even for a large-angle body (e.g., 35-deg sphere cone) with the method of Ref. 8, whereas the present technique with coupling and the Vigneron condition was stable. The Vigneron condition is necessary to obtain stable results even for the first global pass with smaller step sizes (e.g., $\Delta\xi_1 < 0.1$) for both slender and large-angle bodies. The smallest streamwise normalized step size of 0.0134 was used in the present technique, and stable global iterations were obtained. Note that with only coupling of the normal momentum and continuity equations, divergent solutions are obtained when a smaller step size (less than normalized value of 0.1) is employed in the present method and that of Ref. 16.

A comparison of laminar heating distributions computed over a 10-deg blunted cone at a Mach number of 15.44 is presented in Fig. 4. The VSL3D results were presented initially in Ref. 16, and the comparison with the present results is good. In Fig. 5, a comparison with experimental laminar heat-transfer data is provided. The data were measured on a 15-deg blunt cone at a Mach number of 10.6, and the results of the present method are shown to be in good agreement with the data.

Turbulent Flow Comparisons

A comparison of turbulent heat-transfer-rate predictions and experimental data[35] measured over a 9-deg sphere cone at a Mach number of 10.8 is shown in Fig. 6. The hemispherical portion of the model was roughened in order to insure turbulent flow over this region. Three different definitions (described previously) for the boundary-layer-edge locations have been used to calculate turbulent heating with the CS model. The boundary-layer-edge definition based on the gradient of total enthalpy [Eq. (23)] results in heating predictions in agreement with those obtained by the boundary-layer edge defined by the total enthalpy ratio [Eq. (20)]. The predicted heating rates with both edge definitions are in good agreement with the data. For blunt bodies, the total enthalpy ratio has been employed successfully with the CS model in previous turbulent heating studies.[19] The present comparison simply supports the results of Ref. 16 in that the enthalpy gradient is also an

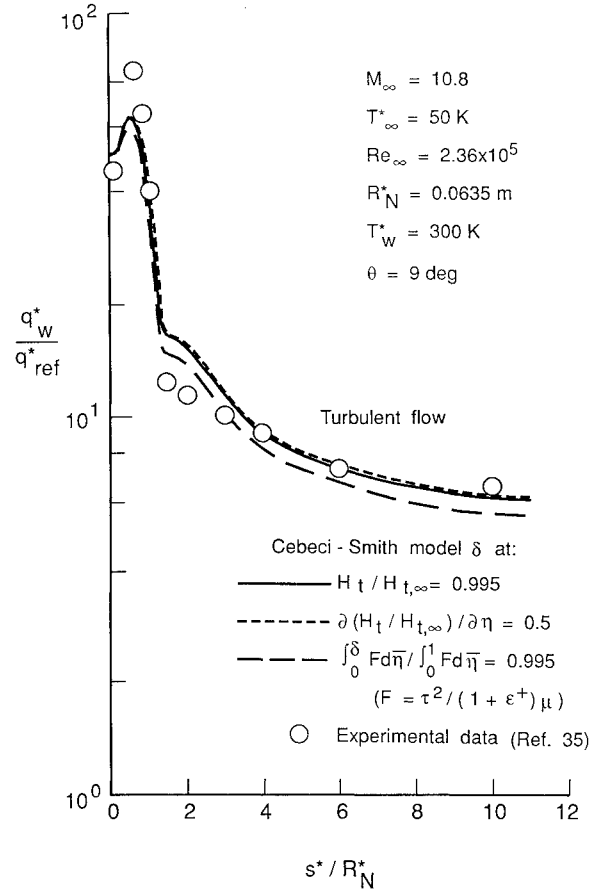

Fig. 6 Surface heat-transfer rate distribution for a 9-deg sphere cone with turbulent flow.

acceptable boundary-layer-edge definition for short blunt bodies. The heating rates computed with the viscous dissipation parameter [(Eqs. (21) and (22)] used to define the boundary-layer edge are approximately 10% lower than the other predictions.

The experimental data presented in Fig. 6 are compared with predicted heating rates based on the BL model in Fig. 7. The original BL model was proposed[23] for constant pressure boundary layers at transonic speeds. This model has been modified as discussed in this study to include the effect of pressure gradient on the damping factor. The predicted heating based on the original model is shown to over-predict the data by approximately 30% on the cone frustum. However, heating predictions based on the present model show significant improvement in comparison with the data, and the comparisons are noted to be similar to those shown for the CS model in Fig. 6.

An experimental Stanton number distribution[36] for turbulent flow obtained on a 7-deg blunt cone at a Mach number of 8 is presented in Fig. 8. Calculated distributions based on the CS and BL models are also shown. The CS model uses the gradient definition of Eq. (23) to determine the boundary-layer edge. In the BL model, the coefficient C_{CP} is used as 1.6. The predicted distributions based on both models are approximately 15% lower than the data. Based on Ref. 27, which used a higher value of the coefficient C_{CP} at supersonic conditions, a value of 3 for this coefficient has been shown[37] to yield good agreement with the data. This trend suggests a Mach number dependence for the coefficient, but more analysis is required since a value of 1.6 was used in the calculated results of Fig. 7 where good agreement was indicated. This coefficient may begin to significantly affect results with the beginning of pressure recovery.

Calculated laminar and turbulent heating-rate distributions over a 5-deg blunt cone at a Mach number of 15 are presented in Fig. 9. The turbulent rates are based on both turbulence models discussed earlier and are obtained with the present

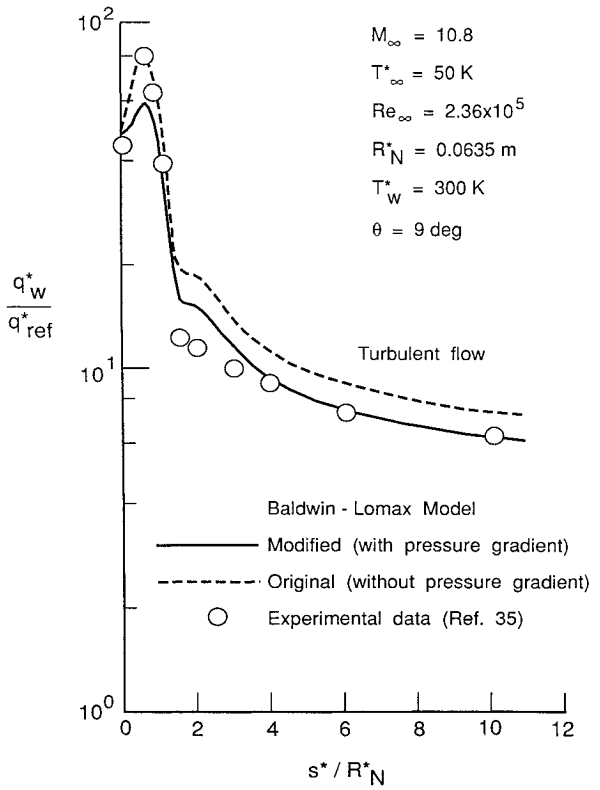

Fig. 7 Surface heat-transfer rate distribution for a 9-deg sphere cone with turbulent flow.

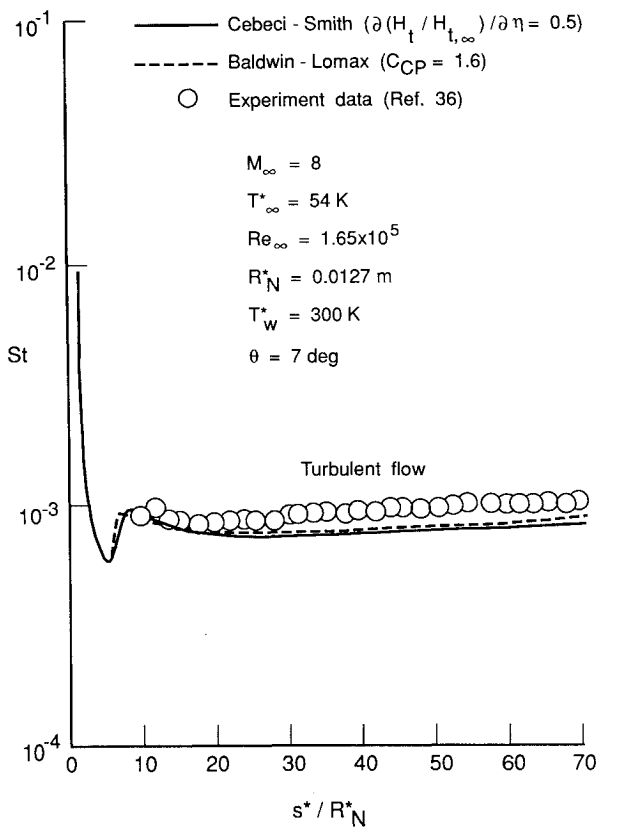

Fig. 8 Stanton number distribution for a 7-deg sphere cone with turbulent flow.

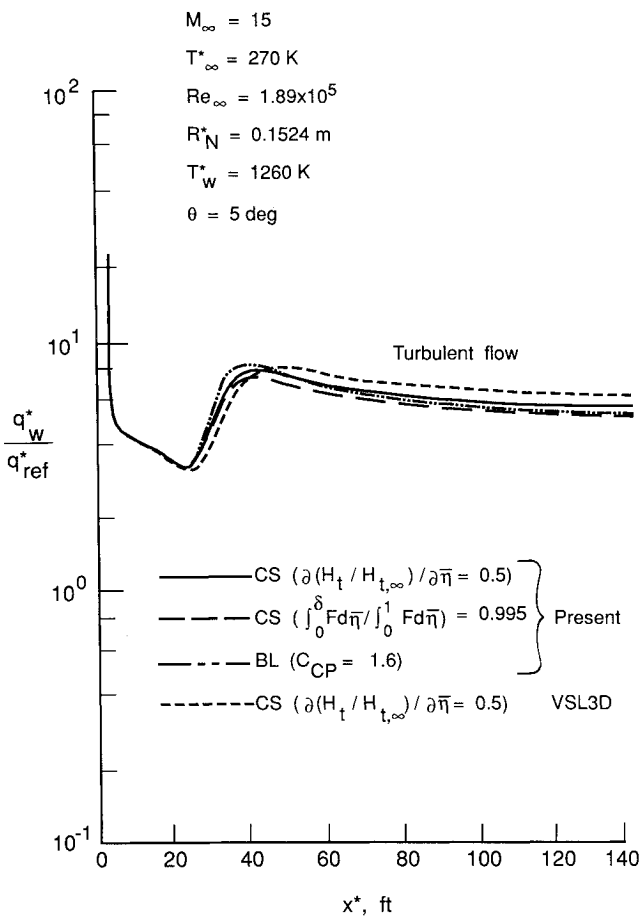

Fig. 9 Surface heat-transfer rate distribution for a 5-deg sphere cone with turbulent flow.

method and the VSL3D method.[15] The values of the computed results obtained from the present method and the two turbulence models are almost the same and are approximately 10–15% lower than the VSL3D values. Again, no significant difference in computed turbulent heating rates is observed for the two models with attached flow conditions.

Concluding Remarks

Numerical solutions from the time-steady viscous shock-layer equations are presented for the hypersonic laminar and turbulent flows over blunted sphere cones. These results are obtained from a viscous shock-layer method that uses coupling between the normal momentum and continuity equations and employs the Vigneron condition with the streamwise pressure gradient in the subsonic nose region.

Detailed comparisons have been made with other predictions and experimental data for slender body flows to assess the accuracy of the present numerical technique. As demonstrated in previous studies, present results also show that a coupling between the normal momentum and continuity equations is essential to obtain solutions past long slender bodies. However, in the method presented here, the use of the Vigneron condition in the subsonic nose region was demonstrated to be necessary to obtain stable global interations with a smaller streamwise step size. Without this condition, departure solutions are encountered with the smaller step sizes. For laminar flow conditions, results of the present method have been shown to be in good agreement with those of other detailed solutions and experimental data.

For turbulent flows, two algebraic turbulence models, namely, the Cebeci-Smith (CS) and the Baldwin-Lomax (BL) models, have been analyzed with the present numerical technique for application to the attached flow conditions over long slender bodies. Both of these models appear adequate for such flows. The CS model is sensitive to the boundary-layer-edge location, and good resolution and accurate solutions near the edge is imperative. A value of 0.5 for the gradient of total enthalpy was shown to provide adequate definition for the edge location. The BL turbulence model avoids the use of a boundary-layer thickness in its formulation and, therefore, does not require finer resolution near the boundary-layer edge. In this study, the BL model has been corrected for the pressure-gradient effects and applied to the hypersonic flow conditions. Improved agreement in some of the comparisons was obtained by modifying a constant in the outer-layer formulation, which may suggest a dependence of this constant on the flow Mach number. Further, comparisons with the experimental data are needed to verify this dependence.

Acknowledgments

This work is dedicated to the memory of Prof. R. T. Davis who passed away on January 25, 1986. Discussions with him, with his insight and deep understanding of the subject, contributed to this work substantially and made its completion possible in this form.

Discussions with Prof. S. G. Rubin and Dr. F. G. Blottner about the Vigneron condition are also acknowledged. Dr. E. C. Anderson provided helpful suggestions on turbulence modeling.

References

[1]Williams, R. M., "National Aerospace Plane: Technology for America's Future," *Aerospace America,* Vol. 24, No. 11, Nov. 1986, pp. 18–22.

[2]Martin, J. A. et al., "Special Section—Orbit-On-Demand Vehicle," *Aerospace America,* Vol. 23, No. 2, Feb. 1985, pp. 46–48.

[3]Lee, K. P., Gupta, R. N., Moss, J. N., Zoby, E. V., and Tiwari, S. N., "Viscous Shock Layer Solutions for the Low Density Hypersonic Flow Past Long Slender Bodies," AIAA Paper 88-0460, Jan. 1988.

[4]Van Dyke, M., "A Review and Extension of Second-Order Hypersonic Boundary Layer Theory," *Rarefied Gas Dynamics,* Fluid Symposium Supplement 2, Vol. II, edited by J. A. Lauermann, Academic, New York, 1963.

[5]Marchand, E. O., Lewis, C. H., and Davis, R. T., "Second-Order Boundary-Layer Effects on a Slender Blunt Cone at Hypersonic Conditions," AIAA Paper 68-54, Jan. 1968.

[6]Vatsa, V. N., Thomas, J. L., and Wedan, B. W., "Navier-Stokes Computations of Prolate Spheroids at Angle of Attack," AIAA Paper 87-2627, 1987.

[7]Gnoffo, P. A., McCandless, R. S., and Yee, H. C., "Enhancements to Program LAURA for Computation of Three-Dimensional Hypersonic Flow," AIAA Paper 87-0280, 1987.

[8]Davis, R. T., "Numerical Solution of the Hypersonic Viscous Shock Layer Equations," *AIAA Journal,* Vol. 8, No. 5, May 1970, pp. 843–851.

[9]Helliwell, W. S., Dickinson, R. P., and Lubard, S. C., "Viscous Flow Over Arbitrary Geometries at High Angle of Attack," AIAA Paper 80-0064, Jan. 1980.

[10]Shanks, S. P., Srinivasan, G. R., and Nicolet, W. G., "AFWAL Parabolized Navier-Stokes Code: Formulation and User's Manual," Air Force Wright Aeronautics Lab., Wright-Patterson AFB, OH, AFWAL-TR-82-3034, June 1982.

[11]Bhutta, B. A., and Lewis, C. H., "Three-Dimensional Hypersonic Nonequilibrium Flows at Large Angles of Attack," AIAA Paper 88-2568, June 1988.

[12]Anderson, D. A., Tannehill, J. C., and Pletcher, R. H., *Computational Fluid Mechanics and Heat Transfer,* McGraw-Hill, New York, 1984.

[13]Werle, M. J., Srivastava, B. N., and Davis, R. T., "Numerical Solutions to the Full Viscous Shock Layer Equations using an ADI Technique," Dept. of Aerospace Engineering, Univ. of Cincinnati, Cincinnati, OH, Rept. AFL-74-7-13, 1974.

[14]Waskiewicz, J. D., Murray A. L, and Lewis, C. H., "Hypersonic Viscous Shock-Layer Flow Over a Highly Cooled Sphere," *AIAA Journal,* Vol. 16, No. 2, 1978, pp. 189–192.

[15]Murray, A. L., and Lewis, C. H., "Hypersonic Three-Dimensional Viscous Shock Layer Flows over Blunt Bodies," *AIAA Journal,* Vol. 16, No. 12, 1978, pp. 1279–1286.

[16]Thompson, R. A., Zoby, E. V., Wurster, K. E., and Gnoffo, P. A., "An Aerothermodynamic Study of Slender Conical Vehicles," AIAA Paper 87-1475, June 1987.

[17]Hosny, W. M., Davis, R. T., and Werle, M. J., "Improvements to the Solution of the Viscous Shock Layer Equations," Arnold Engineering Development Center, Tullahoma, TN, AEDC Rept. TR-79-25, Aug. 1979.

[18]Gordon, R., and Davis, R. T., "An Improved Method for Solving the Viscous Shock Layer Equations," Department of Aerospace Engineering and Engineering Mechanics, Univ. of Cincinnati, Cincinnati, OH, Tech. Rept., Sept. 1985.

[19]Anderson, E. C., and Moss, J. N., "Numerical Solution of the Hypersonic Viscous Shock-Layer Equations for Laminar, Transitional, and Turbulent Flows of a Perfect Gas Over Blunt Axially Symmetric Bodies," NASA TND-7865, Feb. 1975.

[20]Vigneron, Y. C., Rakich, J. V., and Tannehill, J. C., "Calculation of Supersonic Viscous Flow over Delta Wings with Sharp Supersonic Leading Edges," AIAA Paper 78-1137, July 1978.

[21]Davis, R. T. and Blottner, F. G., "A Spatial Marching Technique for the Inviscid Blunt Body Problem," AGARD-CPP-428, April 1987, p. 21.

[22]Cebeci, T., and Smith, A. M. O., *Analysis of Turbulent Boundary Layers,* Academic, New York, 1974.

[23]Baldwin, B. S., and Lomax, H., "Thin Layer Approximation and Algebraic Model for Separated Turbulent Flows," AIAA Paper 78-257, Jan. 1978.

[24]Danberg, J. E., van Gulick, P., and Kim, J., "Turbulence Modeling for Steady Three-Dimensional Supersonic Flows," U. S. Army Ballistic Research Lab., Aberdeen Proving Ground, MD, CR BRL-CR-553, 1986.

[25]Jones, W. P., and Launder, B. E., "The Prediction of Laminarization with a Two-Equation Model of Turbulence," *International Journal of Heat and Mass Transfer,* Vol. 15, No. 2, 1972, p. 301.

[26]Degani, D., and Schiff, L. B., "Computation of Supersonic Viscous Flows Around Pointed Bodies Having Crossflow Separation," *Journal of Computational Physics,* Vol. 66, 1986, pp. 173–196.

[27]Visbal M., and Knight, D., "The Baldwin-Lomax Turbulence Model for Two-Dimensional Shockwave/Boundary-Layer Interactions," *AIAA Journal,* Vol. 22, No. 7, 1984, pp. 921–928.

[28]Dhawan, S., and Narashimha, R., "Some Properties of Boundary Layer Flow During Transition from Laminar to Turbulent Motion," *Journal of Fluid Mechanics,* Vol. 3, Pt. 4, Jan. 1958, pp. 418–436.

[29]Thompson, D. S., and Noack, R. W., "Theoretical and Numerical Study of Departure Behavior in PNS Solutions," *Proceedings of*

the AIAA 8th Computational Fluid Dynamics Conference, AIAA, New York, 1987, p. 237.

[30]Rubin, S. G., "A Review of Marching Procedures for Parabolized Navier-Stokes Equations," *Proceedings of Symposium on Numerical and Physical Aspects of Aerodynamic Flows,* edited by T. Cebeci, Springer-Verlag, New York, 1982, pp. 171-186.

[31]Rubin, S. G., and Lin, A., "Marching with the PNS Equations," *Israel Journal of Technology,* Vol. 18, Nos. 1-2, 1980, pp. 21-31.

[32]Srivastava, B. N., Werle, M. J., and Davis, R. T., "Viscous Shock Layer Solutions for Hypersonic Sphere-Cones," Arnold Engineering Development Center, Tullahoma, TN, AEDC Rept. TR-77-20, Jan. 1977.

[33]Richtmyer, R. D., *Difference Methods for Initial-Value Problems,* Interscience, New York, 1957.

[34]Cleary, J. W., "Effects of Angle of Attack and Bluntness on Laminar Heating-Rate Distributions of a 15 Deg. Cone at a Mach Number of 10.6," NASA TN D-5450, 1969.

[35]Widhopf, G. F., "Turbulent Heat Transfer Measurements on a Blunt Cone at Angle of Attack," Aerospace Corporation, San Bernardino, CA, Aerospace Rept. TR-0059-(S6816-66)-1, Feb. 1971.

[36]Carver, D. B., "Heat Transfer, Surface Pressure and Flow Field Surveys on Conic and Biconic Models with Boundary Layer Trips at Mach 8—Phases IV and VI," Calspan/AEDC Division, Arnold Engineering Development Center, Tullahoma, TN, AEDC-TSR-80-V14, 1980.

[37]Gupta, R. N., Lee, K. P., Moss, J. N., Zoby, E. V., and Tiwari, S. N., "Viscous-Shock-Layer Analysis of Hypersonic Flows Over Long Slender Bodies," AIAA Paper 87-2487, Aug. 1987.

Clark H. Lewis
Associate Editor